JOURNAL OF SPACECRAFT AND ROCKETS
Vol. 47, No. 1, January–February 2010

Description and Flow Assessment of the Delft Hypersonic Ludwieg Tube

Ferry F. J. Schrijer* and Willem J. Bannink†
Delft University of Technology, 2629 HS Delft, The Netherlands

DOI: 10.2514/1.40773

An assessment of the hypersonic Ludwieg tube of Delft University of Technology is given. The facility is described theoretically, and an experimental evaluation is performed to infer the facility performance. Experiments are performed using conventional techniques such as static and total head pressure measurements and Fay–Riddell heat flux evaluations by means of infrared thermography. Furthermore, particle image velocimetry is used to deduce nozzle boundary-layer parameters as well as the freestream velocity field and the static and total temperatures for the Mach 7 nozzle. For the Mach 9 nozzle, stagnation heat flux measurements are performed to obtain the total temperature of the flow. The freestream values were determined experimentally in two different ways and the results showed good agreement. The application of particle image velocimetry allows the freestream flowfield to be directly obtained and gives a direct measure for the flowfield uniformity (0.2%) and repeatability (0.4%). The static and total temperatures calculated from the particle image velocimetry results showed that there is a large mismatch between the theoretical total temperature and measured total temperature, which is attributed to heat losses present in the throat and nozzle.

Nomenclature

A	=	cross section, m^2
a	=	speed of sound, m/s
c_h	=	Stanton number based on $(T_t - T_w)$
c_p	=	heat capacity, J/(kg K)
d, D	=	diameter, m
H	=	boundary-layer shape parameter
H, h	=	enthalpy, J/kg
L	=	length, m
M	=	Mach number
$\dot{P}$	=	expansion rate, s^{-1}
p	=	pressure, bar
q	=	heat flux, W/m^2
R	=	air gas constant, J/(kg K)
Re	=	Reynolds number
r	=	radius, m
St	=	Stanton number based on $(T_t - T_{aw})$
T	=	temperature, K
V, u, v	=	velocity, m/s
x	=	distance, m
γ	=	air specific heat ratio
δ	=	boundary-layer thickness, m
δ^*	=	boundary-layer displacement thickness, m
θ	=	boundary-layer momentum-loss thickness, m
μ	=	viscosity, kg/(m s)
ρ	=	density, kg/m^3
ϕ	=	nozzle half-angle, deg

Subscripts

aw	=	adiabatic wall
e	=	boundary-layer edge
p	=	pitot
s	=	static
t	=	total
w	=	wall
0	=	storage-tube conditions
1	=	reservoir conditions downstream of expansion wave

Superscript

$*$	=	sonic condition

Presented as Paper 3943 at the 26th AIAA Aerodynamic Measurement Technology and Ground Testing Conference, Seattle, WA, 23–26 June 2008; received 3 September 2008; revision received 13 August 2009; accepted for publication 3 November 2009.

*Assistant Professor, Faculty of Aerospace Engineering, Kluyverweg 1.
†Associate Professor (Emeritus), Faculty of Aerospace Engineering, Kluyverweg 1.

I. Introduction

THE flow facility under study is the Hypersonic Test Facility Delft (HTFD), which is a Ludwieg tube with a circular cross section. The Ludwieg tube tunnel concept was first conceived by H. Ludwieg [1] in 1955. Originally, Ludwieg designed the facility as a low cost alternative for subsonic/transonic testing at high Reynolds numbers. The advantage of a Ludwieg tube facility is the ability to create a low-turbulence uniform freestream. Later it was used for hypersonic applications [2,3]. The appeal of this kind of facility to the hypersonic flow regime lies in the relatively long runtimes (0.1 to 0.2 s), large test section (30 cm) and high Reynolds numbers (order of $5–50 \times 10^6$ m^{-1}).

The HTFD was built to be a flexible hypersonic wind tunnel capable of producing relatively high Reynolds numbers within a range of Mach numbers. In addition the facility is designed such that operating costs are minimized (energy and air usage). The basic wind-tunnel design was made by Hyperschall Technologie Göttingen [4] (HTG) in Germany. Sister facilities are in use at the HTG institute itself and at the German University of Bremen. Other hypersonic Ludwieg tubes are the facility at the Technical University of Braunschweig [5] in Germany and the Boeing and U.S. Air Force Office of Scientific Research Mach 6 Quiet Tunnel at Purdue University [6]. The layout of the Bremen Ludwieg tube is similar to the HTFD, whereas the Braunschweig Ludwieg tube uses a single straight tube and has a larger test section. The Purdue University facility has a slightly different setup, since it is specially developed for boundary-layer transition research. The Delft, Braunschweig, and Bremen wind tunnels have a fast-acting valve located upstream of the nozzle, whereas in the Purdue facility, a diaphragm is located downstream of the test section. In the latter facility, boundary-layer suction is applied at the throat to achieve a laminar boundary layer

along the nozzle wall, which reduces the noise in the freestream. However, this is at the cost of larger air usage (the whole test section must be pressurized before the run) and the need of a larger vacuum tank. Furthermore, thicker windows are needed to withstand the high pressures, which makes optical access more difficult.

The measurement of freestream variables has always been challenging in short-duration facilities and is normally performed by means of pressure and temperature heat flux sensors in order to obtain the freestream total pressure, total temperature, and Mach number. Accurate determination of the freestream variables is needed to obtain the Reynolds number and freestream enthalpy. These can be obtained directly by measuring the static flow quantities. As an example, the static pressure is normally obtained by measuring it on a flat plate or cone; however, the value is extremely sensitive to any model misalignment with respect to the freestream. As an alternative, the total values can be used, which then also raises the need for an accurate determination of the Mach number. The static or total temperature is difficult to measure in short-duration facilities, due to the thermal inertia of the probes that are used [7].

During the last two decades, particle image velocimetry has become a standard measurement techniques in the subsonic flow regime and, more recently, has also been applied to supersonic and hypersonic flowfields. The issues related to the application of particle image velocimetry (PIV) in high-speed flows such as recording speed and tracer particle accuracy were addressed by Moraitis and Riethmuller [8] and Kompenhans and Höcker [9]. With the advent of fast interframe charge-coupled-device cameras, the digital version of the technique was successfully applied in the supersonic and hypersonic flow regimes [10–12].

This paper shows the potential of PIV for the calibration of the flow facility. It enables a direct measurement of the freestream velocity field, and through the energy equation, it allows for the calculation of the freestream temperature and the direct nonintrusive measurement of the nozzle-wall boundary layer. Furthermore, a description is given of the operating principle of the Ludwieg tube. Theoretical estimates are given for the runtime, total temperature, and total freestream pressure. Measurements are performed to assess the performance of the facility. Among the measurements are the determination of the wind-tunnel nozzle boundary layer just upstream of the test section and the total wind-tunnel runtime. An accurate determination of the freestream characteristics (total temperature, total pressure, and Mach number) is made for a specified calibration point, and the total operating Mach Reynolds envelope is given. Finally, the effect and limits of freestream condensation are addressed, which are pertinent to these types of facilities.

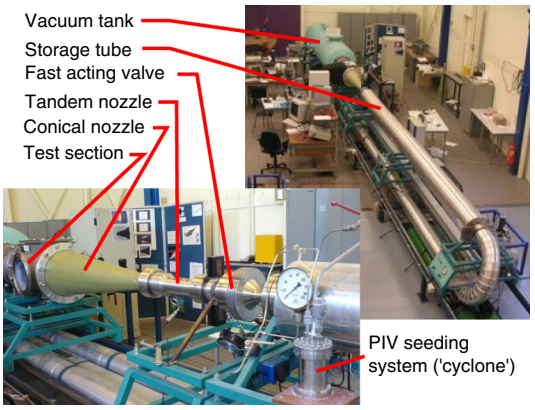

Fig. 1 Overview of the HTFD.

II. Operating Principles of the Ludwieg Tube

The Ludwieg tube consists of four basic sections: storage tube, nozzle, test section, and vacuum tank. The high pressure, high-temperature storage tube is separated from the downstream part of the tube consisting of a nozzle and test section by a fast-opening valve (see Fig. 1). When the valve opens, air flows from the storage tube through the nozzle into the test section. The expansion ratio of the nozzle determines the Mach number in the test section.

The air used in the experiments is stored in the storage tube under high pressure and high temperature. As a result of the opening of the valve, an expansion wave travels into the storage tube. The flow conditions behind the expansion wave act as storage-tube conditions for the flow in the tunnel. Since the valve opening is relatively quick [5], the expansion wave can be described by simple-wave theory [13]. The flow velocity u_1 in the tube can be obtained from

$$\frac{u_1}{a_0} = M_1 \Big/ \left(1 + \frac{\gamma - 1}{2} M_1\right) \tag{1}$$

where

$$u_1 + \frac{2a_1}{\gamma - 1} = \frac{2a_0}{\gamma - 1}$$

along a downstream characteristic (see Fig. 2), a_0 is the speed of sound based on storage-tube conditions, and M_1 is the resulting Mach number in the storage tube.

Region 0 corresponds to the flow conditions in front of the expansion wave, and region 1 corresponds to conditions behind the expansion wave. The total temperature ratio over the expansion wave may be derived as

$$\frac{T_{t,1}}{T_0} = \frac{1 + \frac{\gamma-1}{2} M_1^2}{(1 + \frac{\gamma-1}{2} M_1)^2} \tag{2}$$

corresponding to a total pressure ratio by

$$\frac{p_{t,1}}{p_0} = \left\{ \frac{1 + \frac{\gamma-1}{2} M_1^2}{(1 + \frac{\gamma-1}{2} M_1)^2} \right\}^{\frac{\gamma}{\gamma-1}} \tag{3}$$

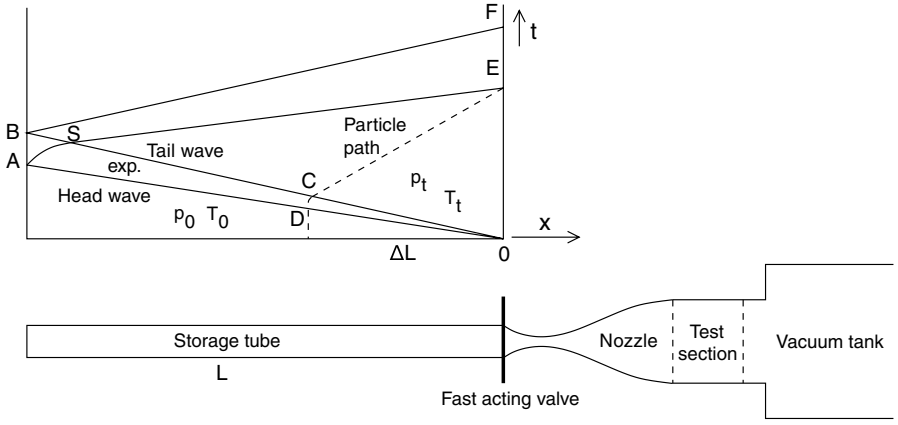

Fig. 2 Operational principle of the Ludwieg tube.

The total running time of the facility with constant storage-tube conditions is governed by the time it takes before the reflected expansion wave returns to the nozzle. It may be calculated as

$$t_1 = \frac{L}{a_0}\frac{2}{1+M_1}\left(1+\frac{\gamma-1}{2}M_1\right)^{\frac{\gamma+1}{2(\gamma-1)}} \tag{4}$$

Finally, the Mach number of the flow downstream of the expansion wave is determined by conservation of mass:

$$\left(\frac{d_{\text{tube}}}{d^*}\right)^2 = \frac{1}{M_1}\left[\frac{2}{\gamma+1}\left(1+\frac{\gamma-1}{2}M_1^2\right)\right]^{\frac{\gamma+1}{2(\gamma-1)}} \tag{5}$$

where the subscript $*$ denotes the critical (sonic) diameter of the throat section. The effects of freestream Mach number on the variation of total quantities and runtime is given in Table 1. For freestream Mach numbers less than 9, a tandem nozzle must be used (see Sec. III, in which the first section consists of the Mach 9 nozzle). Therefore, only the results for Mach numbers 9 and higher are listed. The table shows an increase in losses of total flow quantities and runtime with decreasing Mach number when the Mach 9 case is the most unfavorable. However, it is found that the total temperature loss at the fast-opening valve dominates (see Sec. IV.A).

To prevent condensation in the freestream, the air is heated in the storage tube. To increase the runtime of the tunnel and to reduce the amount of energy required, only a section of the storage tube is heated, which contains the air that is used during the run. The furthest upstream location of a particle that can reach the valve within the runtime (path DCE in Fig. 2) can be approximated by

$$\Delta L = M_1\frac{a_1-u_1}{a_0}2L \tag{6}$$

For a total tube length of $L = 29$ m (see Table 2), a distance of $\Delta L = 5.2$ m results. Therefore, only the first 6 m of the hot tube are heated. To reduce the total length of the facility, the storage tube is divided into three sections consisting of the hot tube and cold tube divided into two parts. The hot tube is connected by means of a bent tube to the first cold-tube section that is located beneath the hot tube and test section. The second cold tube is located next to and connected to the first tube by a 180° bend (see Fig. 3). Since the hot tube is positioned above the cold tube, the problem of convection is minimized.

The temperature in the storage tube has a maximum of 773 K (500°C), due to legislation issues. For high temperatures, the specific heat ratio γ is no longer constant, since the vibrational degree of freedom becomes important. For $T = 773$ K the value for $\gamma = 1.36$ [14], which shows that variations in γ are not important in considering the flow process.

The discontinuity between the high- and low-temperature parts may cause a reflection of the expansion wave unless special precautions are taken. The reflection can be mitigated by changing the tube cross section accordingly, effectively keeping the mass flow constant. Since the cross sections of the hot and cold parts are given (see Table 2), the temperature should be set according to [4]

$$\frac{d_{\text{hot}}}{d_{\text{cold}}} = \left(\frac{T_{\text{cold}}}{T_{\text{hot}}}\right)^{\frac{1}{4}} \tag{7}$$

Hence, for a hot-tube temperature of $T_{\text{hot}} = 773$ K, a cold-tube temperature of $T_{\text{cold}} = 375$ K is needed.

In Fig. 4 a typical pressure variation in time in the storage tube is given. The pressure transducer (Druck Limited PDCR 910 sensor type) is located just upstream of the valve and measures the static pressure (pressure sensor 1 in Fig. 5). Initially, the pressure is equal to the storage-tube pressure, which is $p_0 = 99.8$ bar in this case; subsequently, the pressure drops due to the expansion wave to approximately 83 bar. Since the sensor is flush-mounted with the tube wall, the static pressure p_1 is measured; however, since the Mach number in the tube is low (see Table 1), this is practically equal to the total pressure behind the expansion wave $p_{t,1}$. The rms pressure fluctuation in the storage tube after the expansion wave has passed is 0.3 bar.

After approximately 25 ms a small oscillation is detected, which is caused by a partial reflection coming from the temperature/cross section discontinuity. Progressing further in time, a slow pressure rise is observed, which is attributed to the cold air that is heated under constant volume when it enters the hot tube.

Table 1 Expansion-wave characteristics

M	M_1	$T_{t,1}/T_0$	$p_{t,1}/p_0$	$t_1 a_0/L$
9	0.09	0.97	0.89	1.94
10	0.05	0.98	0.93	1.96
11	0.03	0.99	0.95	1.97

Table 2 HTFD dimensions

Total length of storage tube	$L_{\text{tot}} = 29$ m
Length of hot tube	$L_{\text{hot}} = 6$ m
Length of cold tube	$L_{\text{cold}} = 23$ m
Diameter of test section	$D = 350$ mm
Diameter of hot tube	$D_{\text{hot}} = 49.25$ mm
Diameter of cold tube	$D_{\text{cold}} = 59$ mm

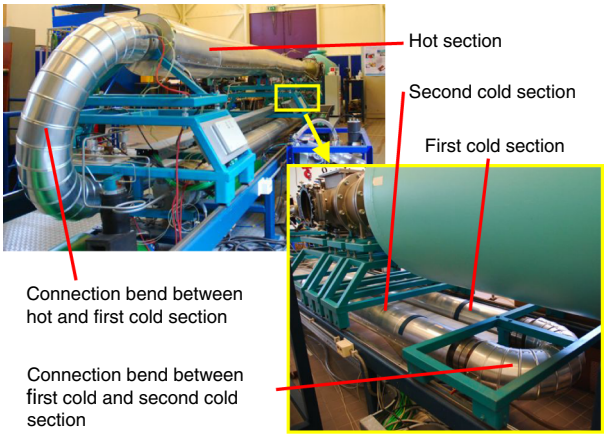

Fig. 3 HTFD storage-tube layout.

III. Nozzle Flow

The nozzle has a conical shape with a 15° total opening angle. The freestream Mach number is varied by changing the throat section. Various throat sections are available (see Table 3). For the Mach 10

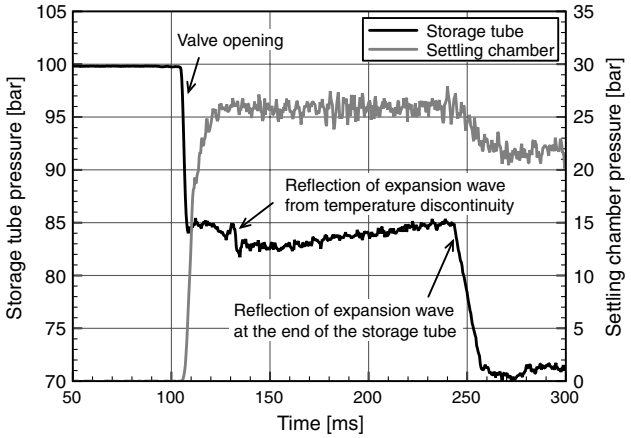

Fig. 4 Pressure variation in time in the hot part of the storage tube and in the settling chamber of the tandem nozzle.

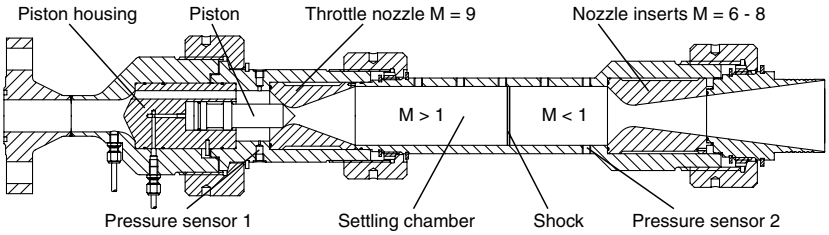

Fig. 5 HTFD tandem nozzle block.

and 11 nozzles, freestream condensation could become a problem; however, since the parts are available for the facility, they are included in the discussion.

For Mach numbers larger than 9, the throat section directly connects to the conical nozzle, and for smaller Mach numbers, an extra throttle nozzle is needed. This is because the throat diameter is limited by the smallest cross section present in the valve. If the throat cross section is larger, sonic conditions in the throat cannot be reached. The first part of the system is a Mach 9 nozzle that accelerates the flow to supersonic speeds after which it is decelerated to subsonic speeds through a number of shocks. The second throat reaccelerates the flow to the desired Mach number (see Fig. 5). Because of the shock waves in the tandem nozzle, a total pressure loss occurs, which can be quantified by considering the total pressure loss over a normal shock wave:

$$\frac{p_{t,2}}{p_{t,1}} = \left(\frac{d_1^*}{d_2^*}\right)^2 \tag{8}$$

In practice, $p_{t,1}$ is the total pressure (downstream of the expansion wave) in the storage tube and $p_{t,2}$ equals the freestream total pressure. The pressure in the settling chamber between the two throats (pressure sensor 2 in Fig. 5) for a freestream Mach number of 7 is measured (Druck Limited PDCR 910 sensor type), the measured signal is indicated in Fig. 4. The measured local static pressure is 25 ± 1 bar. The total pressure is obtained using the local Mach number that is calculated from the ratio of the local cross section (diameter is 70 mm) with respect to the throat cross section. The local Mach number is 0.44; this in combination with the measured static pressure results in a total pressure of $p_{t,2} = 28.8 \pm 1$ bar. The pressure ratio over the throttle nozzle now becomes $p_{t,2}/p_{t,1} = 28.8/83.0 = 0.347$. The geometrical area ratio is $(d_1^*/d_2^*)^2 = (19.35/34.3)^2 = 0.318$; this is slightly lower than the theoretical value. Apparently, the flow in the tandem nozzle block has less total pressure loss than is predicted by normal shock theory.

Downstream of the throat, the nozzle length is determined by the throat-to-test-section area ratio and total opening angle (15°); for Mach 7, this is 1.18 m. Theoretically, the area ratio determines the freestream Mach number. However, in hypersonic facilities, the displacement effect of the nozzle boundary layer can decrease the area ratio, causing a lower freestream Mach number. Commonly, estimates of the boundary-layer thickness are used to correct for these deviations. To determine the boundary-layer thickness at the end of the nozzle, PIV measurements [11,12] were performed for the Mach 7 nozzle. The measurement location is indicated in Fig. 6. A Quantel CFR-PIV-200 Nd:YAG laser (200 mJ pulse energy, 7 ns pulse duration, 532 nm wavelength) was used for illumination. The laser sheet was introduced from the bottom optical access and reflected toward the nozzle wall by means of a mirror that was located in the cavity at the top of the test section. The particle images were recorded by means of a PCO SensiCam QE camera (1376×1040 pixels, 12 bit) with a 105 mm Nikkor objective. TiO_2 tracer particles were used as flow seeding, having a nominal particle size of approximately 500 nm [12,15]. Since the optical access to the nozzle was limited, only a single camera could be placed at a relatively large viewing angle with respect to the illuminated plane (greater than 45°). Although the velocity is less accurate, the relative values still enable a boundary-layer profile to be extracted, to infer the integral boundary-layer quantities. The extracted profile is shown in Fig. 7 with a seventh-order polynomial line fit. The compressible boundary-layer integral quantities were obtained using the turbulent Crocco–Busemann relation relating the velocity profile to the density distribution [16].

Table 3 Throat diameters for the HTFD

M	6	7	8	9	10	11
d^*, mm	48.0	34.3	25.38	19.35	15.12	12.06

A displacement thickness of $\delta^* = 11$ mm was obtained; the rest of the boundary parameters are given in Table 4. In Lukasiewicz [17] an empirical correlation is given for the variation of displacement thickness with the Reynolds number based on the reference temperature:

$$\frac{\delta^*}{x} = 0.42 Re_{\text{ref}}^{-0.2775} \tag{9}$$

When the above correlation is applied to the Mach 7 nozzle for $p_t = 28$ bar and $T_t = 579$ K, a displacement thickness of $\delta^* = 12$ mm results. This agrees well with the measured value of $\delta^* = 11$ mm. The boundary-layer displacement thickness introduces a reduction in the actual area ratio from 104.1 to 85.8, resulting in a Mach number decrease from 7 to 6.7 (see Table 5). This also affects the maximum divergence encountered in the freestream, which decreases from 7.5 to 7.0°.

IV. Freestream Assessment

When the flow enters the test section it continues diverging, due to the outflow from the conical nozzle. Therefore, the flow will expand further and the Mach number in the test section will be higher than that obtained from the theoretical area ratio. For the Mach 7 nozzle, the theoretical Mach number in the test section is computed as $M_{\infty,\text{theory}} = 7.7$. After correcting for the boundary-layer displacement thickness, this is $M_{\infty,\text{cor}} = 7.5$. The local Mach number variation due to the conical flowfield in the center of the test section may be calculated by

$$\frac{\mathrm{d}M}{\mathrm{d}x} = \frac{2M(1 + \frac{\gamma-1}{2}M^2)}{M^2 - 1}\frac{\tan\phi}{r} \tag{10}$$

where ϕ is the nozzle half-angle corrected for the boundary-layer displacement effect and r is the test-section radius, which is obtained from the Mach area-ratio relation. For $M = 7.5$ and $\phi = 7°$, $\mathrm{d}M/\mathrm{d}x = 0.023$ cm^{-1}. For a typical model having a length of $L = 10$ cm, a $\Delta M = 0.23$ results. Since the test section has a cylindrical shape, a shock wave is formed at the nozzle test-section junction (Fig. 6). For $M = 6.7$ (Mach number at the location of the nozzle test-section junction) and a compression angle of $\phi = 7°$, a shock with an angle of $\theta = 14°$ with respect to the freestream is formed, and the shock angle with respect to the test-section wall is 7°.

In Fig. 8 an overview of the vertical component of the freestream flowfield in the test section is shown. The freestream part of the flow was measured using PIV at the location shown in Fig. 6. To visualize the junction shock, the camera was oriented under a large angle with respect to the illuminated plane, requiring a stereo PIV setup. The two component PIV images were recorded using two PCO SensiCam

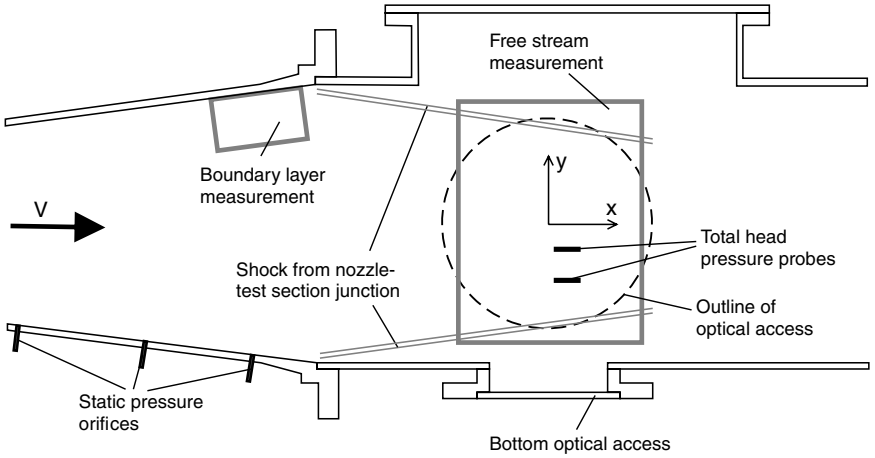

Fig. 6 Side view of the nozzle leading to the test section and test section including the measurement locations.

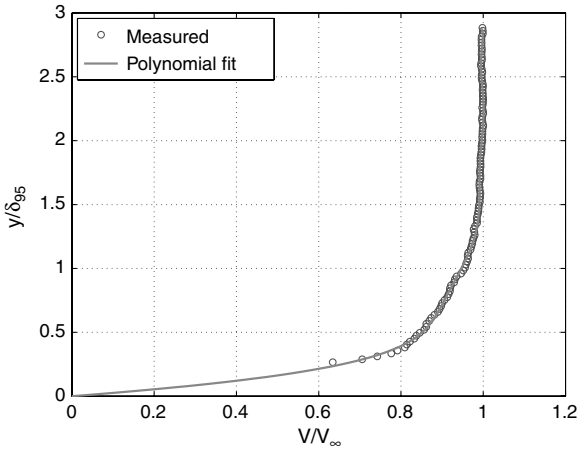

Fig. 7 Boundary-layer profile at the end of the conical Mach 7 nozzle.

QE cameras with 50 mm Nikkor objectives with $f8$. The stereo PIV recordings were performed using four LaVision Imager ProX cameras (2048 × 2048 pixels, 14 bit) with 60 mm Nikkor objectives and $f8$. The laser and seeding was the same as used for the nozzle boundary-layer measurement.

The black circle in Fig. 8 shows the outline of the windows. By plotting the vertical velocity component, the junction shocks are clearly visualized. The shock at the bottom has an angle of 9°, and the angle at the top is 10°. The difference in shock angle between the upper and lower parts of the test section is caused by the presence of a considerably larger cavity at the top, accommodating the model support system. It is thought that the large cavity has a considerable effect on the flow, causing a larger shock angle. However, it has no influence on the freestream flow: in the center of the test section, a region of 200 × 200 mm^2 of undisturbed flow is observed.

The flow divergence caused by the conical nozzle is also clearly measured. A profile of the vertical flow component in the center of the test section is plotted in Fig. 9. The vertical component varies from −60 to +60 m/s over a distance of 200 mm. This complies well with the theoretical divergence corresponding to a total opening angle of 14°, as indicated in Fig. 9.

A profile of the average total velocity magnitude in the center of the test section is given in Fig. 10. The mean velocity is 1033 m/s and the data show a uniformity of 0.2% (rms fluctuations within a single velocity field) and a repeatability of 0.4% (rms fluctuation with different realizations). In Fig. 11 the freestream velocity at the centerline of the test section is given; the increase in velocity with downstream distance is caused by the diverging flow.

Table 4 Boundary-layer parameters for the Mach 7 nozzle flow

Unit Reynolds number	$Re/m = 16.2 \times 10^6$ m^{-1}
95% boundary-layer thickness	$\delta_{95} = 13$ mm
Displacement thickness	$\delta^* = 11$ mm
Momentum-loss thickness	$\theta = 0.63$ mm
Shape parameter	$H = 18$

Table 5 Impact of the boundary layer on nominal wind-tunnel operating conditions

Geometrical cross section	$(A/A^*)_{geo} = 104.1$
Theoretical Mach number	$M_{theory} = 7$
Corrected cross section	$(A/A^*)_{cor} = 85.8$
Corrected Mach number	$M_{cor} = 6.7$

A. Temperature Determination

Since the freestream velocity and Mach number are known, it is possible to deduce the static and total temperature. In hypersonic short-duration facilities, these two quantities are notoriously difficult to determine. However, from the definition of the Mach number, the static temperature can be directly determined:

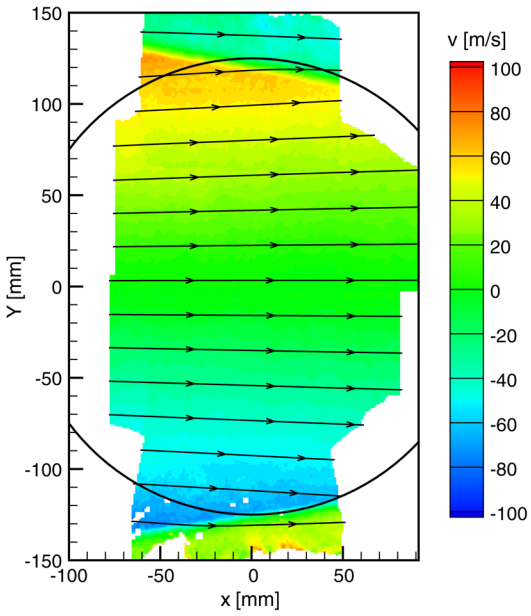

Fig. 8 Vertical velocity component of the freestream flow for the Mach 7 nozzle; measurement location corresponds to the region indicated in Fig. 6.

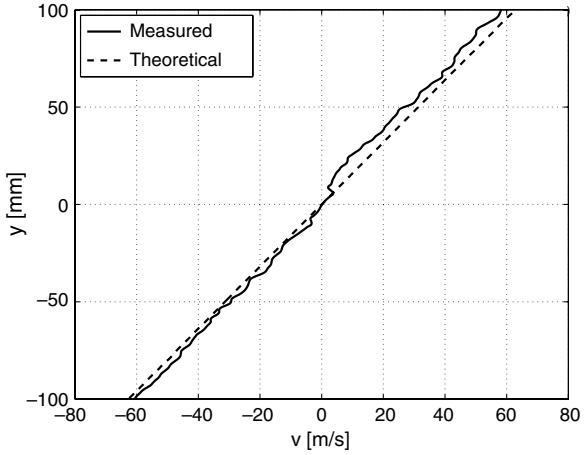

Fig. 9 Flow divergence in the test section for the Mach 7 nozzle; vertical velocity gradient is shown.

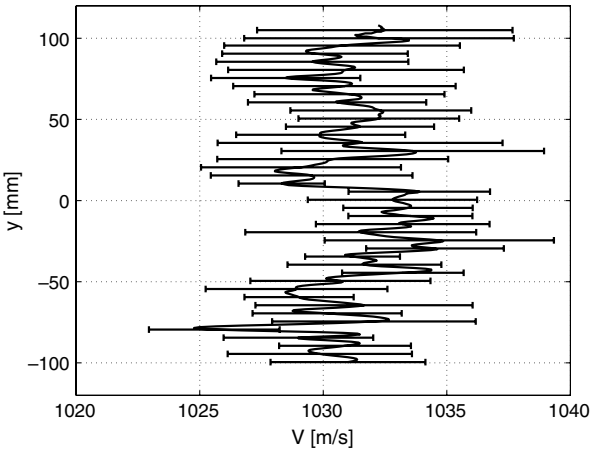

Fig. 10 Vertical profile at $x = 0$ of the freestream velocity for the Mach 7 nozzle.

$$T = \frac{(|V|/M)^2}{\gamma R} \tag{11}$$

The total temperature can now be calculated from the energy equation:

$$T_t = T + \frac{|V|^2}{2c_p} \tag{12}$$

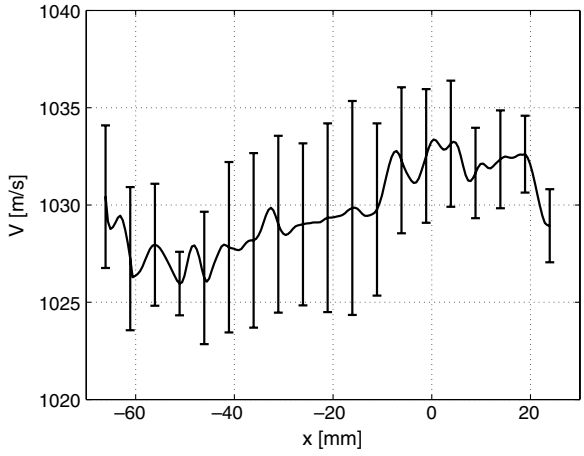

Fig. 11 Horizontal profile at $y = 0$ of the freestream velocity for the Mach 7 nozzle.

Table 6 Freestream temperature for the Mach 7 nozzle

Freestream velocity	$\|V\| = 1033$ m/s
Free static temperature	$T = 47$ K
Free total temperature	$T_t = 579$ K
Free total enthalpy	$H_1 = 0.58$ MJ

The resulting static and total temperatures are given in Table 6. For the determination of the temperatures, the average velocity in the center of the test section is taken in combination with the Mach number that results from the area ratio with boundary-layer correction and pressure measurements (Sec. IV.B).

A discrepancy is observed between the total temperature obtained from Eqs. (11) and (12) and the storage temperature. In Fig. 12 the measured freestream velocity is given by the solid line as a function of the storage-tube temperature, and the dotted line corresponds to the freestream velocity for a fully adiabatic flow, where the total temperature loss over the expansion wave [Eq. (2)] is taken into account. There is a 10% difference between the measured and theoretical velocity. It is thought that losses because of heat transfer in the valve and tandem nozzle are responsible for this.

B. Pressure Measurements

The freestream Mach number and total pressure are alternatively evaluated by means of pressure measurements. Static pressure measurements in the nozzle are performed in combination with pitot tube measurements in the test section using Invensys SCX150AN pressure sensors. The pitot tube formula correlates the measured pitot pressure $p_{t,p}$ to the total pressure $p_{t,1}$ and the local Mach number M_p (at the position of the pitot tube):

$$\frac{p_{t,p}}{p_{t,1}} = \left[\frac{\gamma+1}{2\gamma M_p^2 - (\gamma-1)}\right]^{\frac{1}{\gamma-1}} \left[\frac{(\gamma+1)M_p^2}{(\gamma-1)M_p^2+2}\right]^{\frac{\gamma}{\gamma-1}} \tag{13}$$

The static pressure measurements p_s also correlate the total pressure (which is considered to be constant throughout the nozzle and test section) and the local Mach number M_s:

$$\frac{p_{t,1}}{p} = \left(1 + \frac{\gamma-1}{2} M_s^2\right)^{\frac{\gamma}{\gamma-1}} \tag{14}$$

To be able to solve the two equations, it is assumed that the flow divergence is equal to the inviscid case corrected for the boundary-layer displacement thickness. Now the local Mach number at the location of the static pressure orifices in the nozzle wall can be related to the Mach number at the pitot tubes using the nozzle opening angle and the distance Δx between the static pressure orifices and pitot tubes. From geometry relations, it follows that

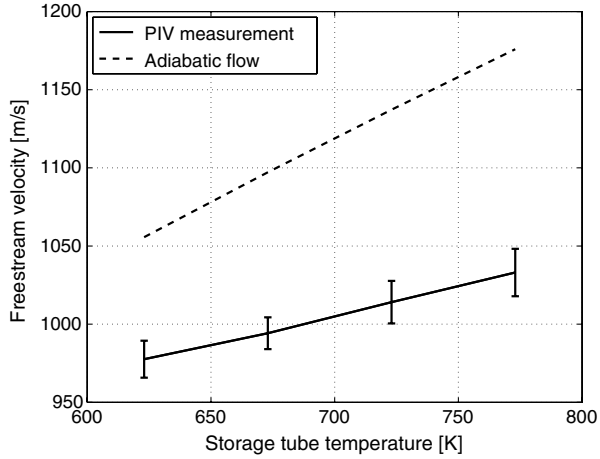

Fig. 12 Variation of measured and theoretical freestream velocity with storage-tube temperature for the Mach 7 nozzle.

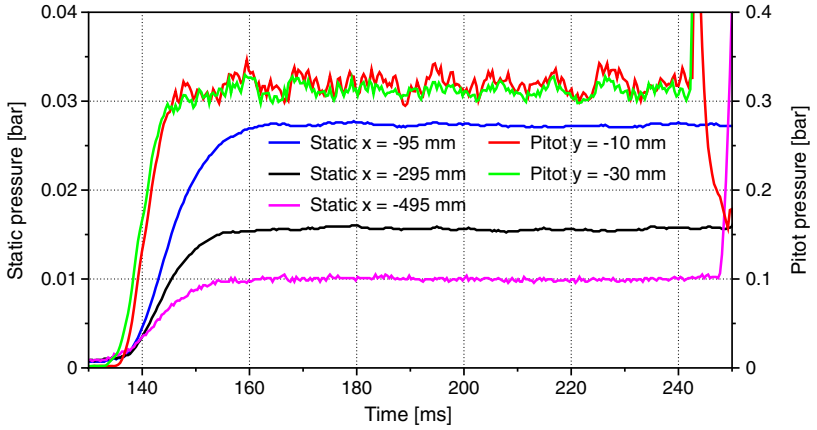

Fig. 13 Static and pitot pressure variation in time for the Mach 7 nozzle.

$$\frac{A_s}{A^*} = \left(\frac{r^* \sqrt{(A_p/A^*)} - \Delta x \tan \phi}{r^*} \right)^2 \tag{15}$$

where the local Mach number is related to the local cross section by the Mach area-ratio relation. Finally, the equations are solved for p_t and M_r.

In the measurements, static pressure taps were installed at 95, 295, and 495 mm from the nozzle test-section junction (see Fig. 6). Simultaneously, a pitot probe was installed in the test section, located 300 mm downstream of the junction. In the current procedure, three static pressure signals are used in combination with two pitot pressure signals in the optimization for finding p_t and M_p. For the pressure signals given in Fig. 13, the following average values are obtained: $M_p = 7.5 \pm 0.1$ and $p_t = 27.9 \pm 1$ bar (see also Table 7).

C. Stagnation Heat Flux Measurements

To determine the freestream temperature for the nozzle setup without the tandem nozzle configuration, the stagnation heat flux on a 50-mm-radius sphere cylinder was measured by means of infrared thermography. Because of the presence of seeding particles in the flow, condensation occurred for the $M = 9$ nozzle, which prevents the static and total temperatures from being determined by means of PIV. The thermograms were obtained using an Agema Thermovision 880 long-wave-band infrared scanner (20 mK noise equivalent temperature difference) modified to work at 2.5 kHz in line-scan mode. In Fig. 14 the heat flux variation in time is shown for different Reynolds numbers (total pressures).

The horizontal lines in Fig. 14 are the theoretical values obtained using the Fay–Riddell stagnation-point heat transfer correlation [18]. The temperature difference used to compute c_h in Fig. 12 is $T_t - T_w$, since the adiabatic-wall temperature is difficult to obtain accurately within such short runtimes. Therefore, the Fay–Riddell Stanton number was also normalized using $T_t - T_w$:

$$c_h = St \frac{T_t - T_{\text{aw}}}{T_t - T_w} \tag{16}$$

The total temperature was varied to fit the Fay–Riddell results to the measured heat flux. The best agreement was found for $T_t = 585$ K, which corresponds well to the total temperature for the $M = 7$ nozzle. The total temperature measured is marginally higher than for the $M = 7$ nozzle which was 579 K. This is attributed to the fact that

Table 7 Average measured pressure with the resulting Mach number and total pressure

$p_{s,1}$, bar	$p_{s,2}$, bar	$p_{s,3}$, bar	$p_{p,1}$, bar	$p_{p,2}$, bar	M	p_t, bar
0.0100	0.0156	0.0273	0.3123	0.3197	7.5	27.9

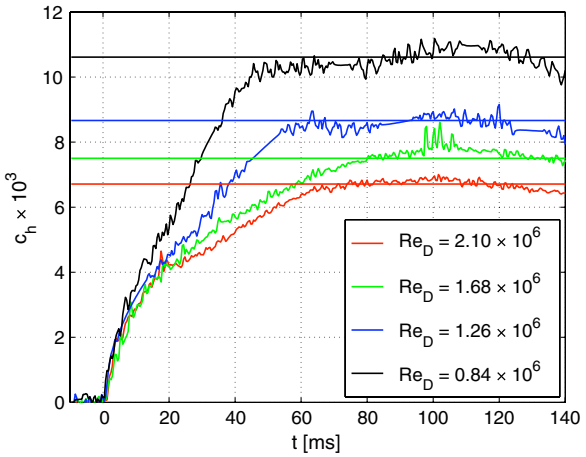

Fig. 14 Measured stagnation-point heat transfer compared with Fay–Riddell correlation results.

no tandem nozzle is required, thus reducing the amount of heat lost in the process.

D. Comparison Between Predictions and Measured Results

The wind tunnel was extensively operated with the Mach 7 nozzle at a storage-tube pressure of 100 bar and a storage temperature of 773 K. The displacement effect of the boundary layer was measured and the effect on the freestream Mach number was evaluated. Simultaneously, the Mach number was obtained from static and pitot tube measurements (Sec. IV). Both evaluations agreed on a test-section Mach number of $M = 7.5$. The total pressure was inferred from the static pitot pressure measurements and the pressure measured just upstream of the second throat; the result was a total pressure of $p_t = 27.9$ bar (Sec. III). The freestream velocity was used to calculate the freestream total temperature $T_t = 579$ K. In the

Table 8 Overview of methods to assess the freestream characteristics of the HTFD at a storage pressure of 100 bar and storage temperature of 773 K

Measurement method	Value
Mach number M	
Theory with boundary-layer correction	7.5 ± 0.1
Static pitot pressure measurement	7.5 ± 0.1
Total pressure p_t, bar	
Pressure upstream of the throat	28.6 ± 1
Static pitot pressure measurement	27.9 ± 1
Total temperature T_t, K	
Velocity by means of PIV in $M = 7$ nozzle	579
Fay–Riddell evaluation in $M = 9$ nozzle	585

case of the Mach 9 nozzle, a total temperature of $T_t = 585$ was obtained by means of Fay–Riddell evaluations. For an overview of the methods used to determine the freestream variables, see Table 8.

E. Operational Envelope

The freestream characteristics for the Mach 7 nozzle are used to establish the Mach Reynolds operational envelope of the HTFD. The freestream Mach number is obtained from the theoretical area ratio corrected for the displacement effect of the nozzle boundary layer. Equation (9) is used in combination with the conditions of the Mach 7 nozzle and a total pressure of 28 bar in order to obtain the displacement thickness at other Mach numbers and total pressures:

$$\frac{\delta^*}{(\delta^*)_{M7}} = \left\{\frac{Re_{\text{ref}}}{(Re_{\text{ref}})_{M7}}\right\}^{-0.2775} \tag{17}$$

The maximum total pressure is determined by the maximum allowable pressure in the storage tube and the losses when the tandem nozzle is installed. The minimum pressure is determined by the pressure ratio needed to operate the tunnel at the given Mach number. The total temperature is $T_t = 585$ K without the tandem nozzle and $T_t = 579$ K with the tandem nozzle installed.

The freestream total quantities as well as Mach and unit Reynolds number for different nozzle geometries are given in Table 9 and in Fig. 15. The total temperature is fixed at the maximum allowed to prevent condensation issues; however, for the lower Mach numbers ($M = 6$ and 7 nozzles), the temperature could be reduced to achieve a higher Reynolds number. As can be observed, the unit Reynolds number increases with the freestream Mach number up to the Mach 9 nozzle; this is because the pressure loss in the tandem nozzle decreases. For the Mach 10 nozzle, the unit Reynolds number decreases, as expected from theory.

F. Condensation

Since the freestream static temperature is relatively low, it should be carefully verified that the flow is not affected by condensation effects. In general, two types of condensation processes are possible: heterogeneous condensation, which behaves like equilibrium condensation, and spontaneous condensation, for which supercooling is possible. Heterogeneous condensation is characterized by the process with which the degree of CO_2 and H_2O content in air is sufficient to cause condensation of nitrogen and oxygen around the existing nuclei. Spontaneous condensation is characterized by the nucleation of nitrogen molecules, which then act as nuclei for the rest of the nitrogen and oxygen. The spontaneous-condensation process is governed by the ratio of expansion rate to static pressure, $\dot{P}/p$ [19], which indicates the possible amount of supercooling. For the HTFD freestream, this quantity is given by

Table 9 Freestream total quantities for different nozzles and total pressures

M	p_t, bar	T_t, K	$Re/m \times 10^6$, m^{-1}
		$M = 6$ *nozzle*	
6.4	2.8	579	1.61
6.5	14.3	579	7.90
		$M = 7$ *nozzle*	
7.4	5.4	579	2.22
7.5	28.0	579	11.05
		$M = 8$ *nozzle*	
8.4	10.0	579	3.07
8.5	51.2	579	15.08
		$M = 9$ *nozzle*	
9.4	20	585	4.65
9.5	88	585	19.70
		$M = 10$ *nozzle*	
10.3	20	585	3.76
10.5	88	585	15.85

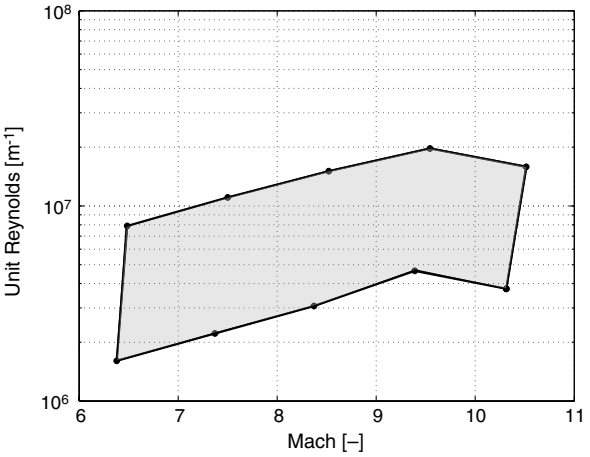

Fig. 15 Operational Mach Reynolds envelope.

$$\frac{\dot{P}}{p} = \frac{\sqrt{\gamma R T_t}}{p_t}\frac{2\gamma M^4}{M^2 - 1}\frac{r\tan\phi}{r^{*2}} \tag{18}$$

where $\dot{P} = -(1/p)(\mathrm{d}p/\mathrm{d}t)$, r is the local radius, and r^* is the throat radius. In case $\dot{P}/p$ is smaller than about 0.1–1 s^{-1} mbar^{-1}, little or no supercooling is expected, since the process is dominated by heterogeneous condensation. For HTFD the value of $\dot{P}/p$ is around 3–50 s^{-1} (mbar)$^{-1}$, where the high values are obtained for the higher Mach numbers. From this, it can be concluded that the condensation process is dominated by spontaneous condensation and supersaturated conditions can be achieved.

In Fig. 16 a pressure–temperature diagram is given in which data are depicted for condensation onset in hypersonic facilities [19]. In the figure, the mean onset of nitrogen as obtained from experiments is also shown. In general, the expansion rate decreases with increasing nozzle size; therefore, the amount of supercooling for large facilities is reduced, resulting in an earlier condensation onset [17]. For low static pressures ($\approx$1 mbar), the seeding effects of CO_2 and H_2O are negligible and spontaneous condensation dominates the process. The black dots indicate the HTFD static conditions at different Mach numbers. For the $M = 7$ nozzle, the static conditions are still within the equilibrium condensation limits for N_2. At higher Mach numbers, static temperatures are achieved for which equilibrium condensation would occur. However, previous experience with the $M = 9$ nozzle also shows that this configuration achieves a freestream without condensation. Additionally, it may be remarked that the Purdue and Braunschweig facilities operate under similar relatively low-stagnation conditions in which also supercooling has been observed.

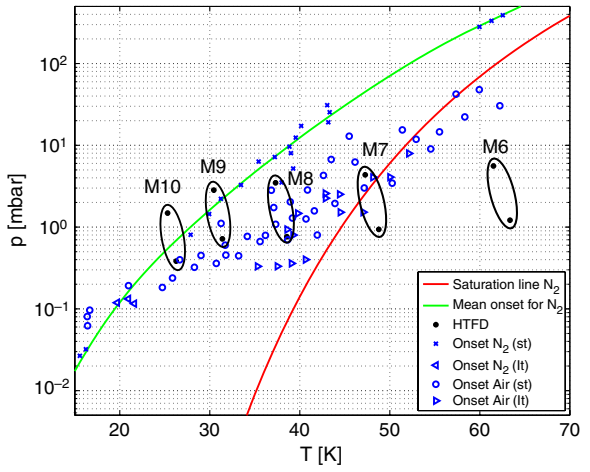

Fig. 16 Experimental estimates of condensation onset, data taken from Daum and Gyarmathy [19] and Lukasiewicz [17]; st means small tunnel (less than 30 cm) and lt means large tunnel (greater than 130 cm).

V. Conclusions

The layout and working principle of the Hypersonic Test Facility Delft (HTFD) has been given. The facility has a running time of approximately 100 ms and can operate at a range of Mach numbers. The performance of the facility was verified against theory by means of pressure measurements, velocity measurements by means of PIV, and infrared thermography.

For the $M = 7$ nozzle, the freestream Mach number, total pressure, and total temperature were all determined in two independent ways. The nozzle boundary-layer displacement thickness was measured by means of PIV and used to correct the geometrical cross section for the determination of the freestream Mach number. Additionally, it was also inferred from static pressure measurements at the nozzle wall in combination with pitot pressure measurements in the test section. These measurements also allowed the total freestream pressure to be obtained. It was found that this matched the total pressure measured in the tandem nozzle. The total and static temperature was obtained from PIV velocity measurements for the $M = 7$ nozzle. In the case of the $M = 9$ nozzle, the total temperature was obtained using Fay–Riddell evaluation. Furthermore, the application of PIV also allowed to infer the freestream uniformity and repeatability.

It was shown that the experimental achievements as obtained by the mechanical quantities pressure and Mach number met the predicted theoretical expectations. However, the temperature did not come off as favorable. The total temperature obtained from the PIV velocity measurements and the Mach number using the Mach area-ratio relation was 579 K, and the expected temperature was 750 K. This deficiency may be attributed to the large unknown heat transfer at the passage of the flow from the storage tube via the complex mechanism containing the fast-acting valve to the nozzle. This aspect is possibly addressed unsatisfactorily in the literature of facilities similar to the present one.

Using the freestream characteristics for the Mach 7 nozzle, a Mach Reynolds envelope was established ranging from $M = 6.5$ to 10.5 with unit Reynolds numbers ranging from $Re/m = 1.61 \times 10^6$ at $M = 6.5$ until $Re/m = 19.70 \times 10^6$ at $M = 9.5$.

Acknowledgments

This work is supported by the Dutch Technology Foundation STW under the VIDI Innovation Impulse program, grant DLR.6198. The authors would like to acknowledge F. Scarano for his advice and they also thank R. Caljouw for his help in performing the experiments.

References

[1] Ludwieg, H., "Der Rohrwindkanal," *Zeitschrift für Flugwissenschaften*, Vol. 3, 1955, pp. 206–216.

[2] Hottner, T., "Der Rohrwindkanal der Aerodynamischen Versuchsanstalt Göttingen," Aerodynamischen Versuchsanstalt, TR 68A 77, Göttingen, Germany 1968.

[3] Hottner, T., "Eichmessungen im Rohrwindkanal 500 Ø der AVA," Aerodynamischen Versuchsanstalt, TR 69A23, Göttingen, Germany 1969.

[4] Friehmelt, H., Koppenwallner, G., and Muller-Eigner, R., "Calibration and First Results of a Redesigned Ludwieg Expansion Tube," AIAA Paper 93-5001, 1993.

[5] Wolf, T., Estorf, M., and Radespiel, R., "Investigation of the Starting Process in a Ludwieg Tube," *Theoretical and Computational Fluid Dynamics*, Vol. 21, No. 2, 2007, pp. 81–98. doi:10.1007/s00162-006-0040-z

[6] Juliano, T., Schneider, S., Aradag, S., and Knight, D., "Quiet-Flow Ludwieg Tube for Hypersonic Transition Research," *AIAA Journal*, Vol. 46, No. 7, 2008, pp. 1757–1763. doi:10.2514/1.34640

[7] Estorf, M., Wolf, T., and Radespiel, R., "Experimental and Numerical Investigations on the Operation of the Hypersonic Ludwieg Tube Braunschweig," *Proceedings of the Fifth European Symposium on Aerothermodynamics for Space Vehicles*, ESA Special Publications, Vol. 563, Cologne, Germany, 2004, pp. 579–586.

[8] Moraitis, C., and Riethmuller, M., "Particle Image Displacement Velocimetry Applied in High-Speed Flows," *4th International Symposium on Application of Laser Anemometry to Fluid Dynamics*, Lisbon, Portugal, 1988.

[9] Kompenhans, J., and Höcker, R., "Application of Particle Image Velocimetry to High-Speed Flows," VKI Lecture Series, von Karman Inst. for Fluid Dynamics, Rhode-St.-Genese, Belgium, 1988.

[10] Havermann, M., Haertig, J., Rey, C., and George, A., "Application of Particle Image Velocimetry to High-Speed Supersonic Flows in a Shock Tunnel," 11th International Symposium on Application of Laser Technology to Fluid Mechanics, Paper 4.4, Lisbon, Portugal, 2002.

[11] Scarano, F., and van Oudheusden, B., "Planar Velocity Measurements of a Two-Dimensional Compressible Wake," *Experiments in Fluids*, Vol. 34, No. 3, 2003, pp. 430–441.

[12] Schrijer, F., Scarano, F., and van Oudheusden, B., "Application of PIV in a Mach 7 Double-Ramp Flow," *Experiments in Fluids*, Vol. 41, 2006, pp. 353–363. doi:10.1007/s00348-006-0140-y

[13] Liepmann, H., and Roshko, A., *Elements of Gasdynamics*, Dover, New York, 2001.

[14] Staff, A. R., "Equations, Tables, and Charts for Compressible Flow," NACA, Rept. 1135, 1953.

[15] Schrijer, F., and Scarano, F., "Particle Slip Compensation in Steady Compressible Flows," *Proceedings of the 7th International Symposium on Particle Image Velocimetry*, Rome, 2007, pp. 1–6.

[16] White, F. M., *Viscous Fluid Flow*, 2nd ed., McGraw–Hill, Singapore, 1991.

[17] Lukasiewicz, J., *Experimental Methods of Hypersonics*, Vol. 3, Marcel Dekker, New York, 1973.

[18] Anderson, J. D., *Hypersonic and High Temperature Gas Dynamics*, AIAA Education Series, AIAA, Reston, VA, 2006.

[19] Daum, F., and Gyarmathy, G., "Condensation of Air and Nitrogen in Hypersonic Wind Tunnels," *AIAA Journal*, Vol. 6, No. 3, 1968, pp. 458–465. doi:10.2514/3.4520

T. Lin
Associate Editor